A Geometry-Based Modelling Approach for the Line-of-Sight Probability in UAV Communications

ABDUL SABOOR [1], EVGENII VINOGRADOV [1,2] (Member, IEEE),
ZHUANGZHUANG CUI [1] (Member, IEEE), AKRAM AL-HOURANI [3] (Senior Member, IEEE),
AND SOFIE POLLIN [1,4] (Senior Member, IEEE)

[1]WaveCoRE, Department of Electrical Engineering, KU Leuven, 3000 Leuven, Belgium

[2]Autonomous Robotics Research Center, Technology Innovation Institute, Abu Dhabi, UAE

[3]School of Engineering, RMIT University, Melbourne, VIC 3000, Australia

[4]IMEC, 3001 Leuven, Belgium

CORRESPONDING AUTHOR: A. SABOOR (e-mail: abdul.saboor@kuleuven.be)

This work was supported by the Research Foundation Flanders (FWO) under Project G098020N.

ABSTRACT This paper presents a geometry-based three-dimensional Probability of Line of Sight (P_{LoS}) model for generic urban environments. The existing P_{LoS} models are mostly empirical, based on measurements or ray-tracing simulations at specific environments. To enable Unmanned Aerial Vehicle (UAV) communication in various environments, it is urgently necessary to develop an analytical model with high parameter scalability. Through introducing the ITU model that describes a built-up environment with three parameters, we derive a closed-form P_{LoS} model with the inputs of city built-up parameters, UAV altitude, elevation θ and azimuth φ angles between UAV and User Equipment (UE). Furthermore, we develop a geometry-based simulator to validate the proposed analytical model. The results show good agreements between the simulated results, analytical results, and 3GPP P_{LoS} measurements. We demonstrate that the existing models provide less accurate results, which calls for re-evaluating the use cases and performance of UAV-mounted communication equipment in urban environments.

INDEX TERMS 3D model, line of sight (LoS), probability of line of sight (P_{LoS}) model, unmanned aerial vehicles (UAV), UAVs as NodeB (UxNB).

I. INTRODUCTION

IN THE recent years, Unmanned Aerial Vehicles (UAVs) have become popular in both military and civilian domains [1], [2], [3]. The primary reasons for their increasing popularity are their flexible maneuverability, rapid deployment, and low cost [4], [5], [6]. Because of these advantages, UAVs as NodeB (UxNBs) are considered to provide coverage in emergent scenarios, such as disaster relief, infrastructure-shortage areas, or hot-spot ultra-dense areas where Ground NodeBs (GNBs) are insufficient to meet communication demands [7], [8].

In addition to earlier advantages, the UxNBs have better Line-of-Sight (LoS) probability to ground User Equipment (UE) when compared to GNB [9]. The availability of LoS links significantly improves the performance of communication systems, especially for high-altitude Air-to-Ground

(A2G) communication. For example, the transmit signal from UxNB at higher altitudes will be extremely weak at the UEs if a LoS link is obstructed [10], [11]. At the same time, The LoS probability is an indispensable part of large-scale channel modeling, which is vital for trajectory planning, handover, and coverage analysis [12]. Therefore, it is necessary to accurately model the LoS Probability (P_{LoS}), particularly for urban environments with many buildings to disrupt LoS links.

UxNBs are envisioned to play a pivotal role in addressing coverage needs within urban environments, especially where conventional infrastructure deployment is challenging or when catering to high user demands [13]. However, a major hurdle in such environments is the obstruction of the LoS connectivity between UxNBs and UEs due to architectural structures such as buildings [14]. Research

by Rodriguez et al. [15] highlights that these buildings can introduce huge signal attenuation, potentially reaching up to 40 dB, depending upon factors like frequency and building composition materials. This situation leads to frequent interruptions in the services. Therefore, it is essential to understand LoS behavior in different urban environments.

A. OVERVIEW OF P_{LoS} MODELING APPROACHES

Several widely used P_{LoS} models exist in literature. For example, International Telecommunication Union (ITU) report M.2135-1 provides P_{LoS} model for Urban Micro (UMi) and Urban Macro (UMa) environments [16]. Similarly, the Third-Generation Partnership Project (3GPP) derives P_{LoS} model for the UMa environment based on measurements in TR 38.900 [17]. A few more popular P_{LoS} models are presented in [18], [19]. However, all the above-mentioned P_{LoS} models are mainly designed for terrestrial communications with traditional GNBs. In reality, the UxNB flies at higher altitudes with 3D mobility, thus requiring modifications in the standard P_{LoS} model.

In the A2G context, numerous P_{LoS} models have been proposed in existing works, which can be divided into deterministic, empirical, and geometry-based models. The deterministic models are obtained by Ray Tracing (RT) simulations conducted in three-dimensional (3D) digital models of real urban environments [20], [21]. Therefore, RT-based deterministic models can provide accurate results for an underlying environment using exhaustive computation, which requires expensive high-end hardware. As a result, RT simulations increase the computational complexity and overall cost, limiting the models' scalability [22].

Empirical models are created from real-world measurement or simulator data, helping us understand network behavior [17], [23], [24], [25], [26]. Such models are specific to the conditions under which the data was collected, making them less applicable in diverse environments. Therefore, such models only support limited height and a limited set of environments. Furthermore, empirical models can be time-consuming to be constructed due to the need for extensive field measurements.

Lastly, the geometry-based LoS model relies on the spatial arrangement of objects in the environment to predict whether a direct line between the UxNB and UE is obstructed [27], [28], [29], [30]. It uses readily available geometric data to estimate P_{LoS}, making it a cost-efficient solution, particularly in scenarios where detailed material information or complex simulations are not feasible [31]. One of the key advantages of geometry-based models is their versatility and adaptability across various environments and changing conditions. Therefore, despite their simplicity, geometry-based models often provide a reasonable approximation of P_{LoS} in diverse real-world situations, making them valuable tools in wireless communication planning and optimization.

B. OVERVIEW OF GEOMETRY-BASED P_{LOS} APPROACHES

The Manhattan Grid stands out in wireless communication due to its ability to provide a simplified yet effective representation of the complex urban environment for easily analyzing and optimizing wireless networks for urban environments. It breaks down complex urban environments into a regular grid pattern, facilitating easier signal propagation analysis. Furthermore, its versatility allows for its application across diverse urban environments, enhancing its utility in assessing wireless network performance.

Several State-of-The-Art (SOTA) P_{LoS} models use the Manhattan Grid structure for P_{LoS}. Most of these models are derived from model [32] conceived by the ITU. For example, Al-Hourani et al. [25] used the ITU model to derive a closed-form empirical P_{LoS} model and used it four standard urban environments, suburban, urban, dense urban, and high-rise. After that, various geometry-based A2G P_{LoS} models are presented in [28], [29], [30] using a built-up environment defined by ITU. Authors in [28] use the Fresnel clearance zone to fine-tune LoS calculations for different frequencies. Reference [29] uses the same geometry to forecast the behavior of LoS, ground specular, and building scattering BS paths in A2G communications. The authors of [30] emphasized that the ITU modeling approach in [32] only considers elevation angle while the azimuth is not taken into account. To bridge the gap, [30] proposes a 3D modeling approach and provides lower and upper bounds on the probability of LoS being blocked by the closest building.

On the other hand, some studies, such as [10], [11], [27], propose alternative city layouts. In [27], the model employs Poisson Point Processes (PPPs) to generate street origins, followed by the formulation of buildings based on average street widths. By offering closed-form expressions for the P_{LoS} across diverse building height distributions and spatial orientations, the model demonstrates its flexibility in assessing various urban layouts from suburban to high-rise scenarios. Works in [10], [11] model obstacles as random points following the PPP. Next, the obstacles are represented as cylinders of a fixed radius and a random height. This geometry is used to derive LoS probability using a simplified exponential relation.

1) LIMITATIONS OF THE EXISTING MODELS

All ITU-inspired models in [10], [11], [25], [28], [29], [32] are based on two assumptions regarding UE and UxNB locations (see Fig. 1(a)):

- The street width separates UE from the closest building potentially affecting LoS.
- The UE-UxNB link is aligned with the Manhattan Grid (i.e., azimuth $\varphi = 0$ is merely assumed).

As it is emphasized in [26], [30], [33], these assumptions are not realistic and have a significant effect on resultant P_{LoS}. While the authors of [26], [30] tried to tackle these issues, their models do not explicitly contain azimuth. Moreover, despite its elaborated methodology, the model
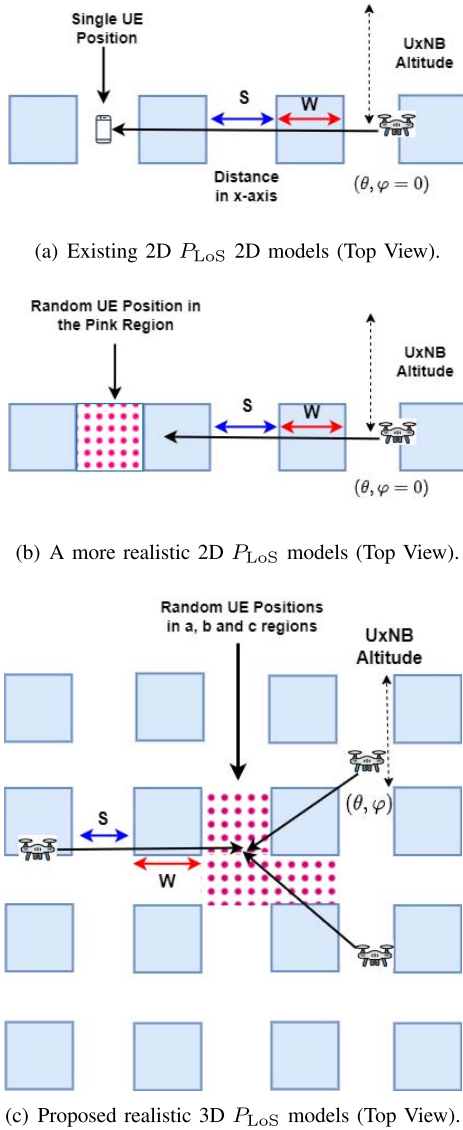
(a) Existing 2D P_{LoS} 2D models (Top View).

(b) A more realistic 2D P_{LoS} models (Top View).

(c) Proposed realistic 3D P_{LoS} models (Top View).

FIGURE 1. P_{LoS} calculation method in the proposed and existing models.

in [30] considers only the blockage effect of the closest building while [26] uses a methodology that cannot produce results for environments beyond the standard ones with fixed sets of build-up parameters.

Models in [10], [11], [27] use alternate city layouts, making them challenging for standardization purposes. P_{LoS} models in [10], [11] cannot reproduce azimuth-dependent P_{LoS} behavior as they take only the height of each point and the distance between them as input. Additionally, both the above-mentioned models use empirical fitting parameters. Thus, extending their P_{LoS} models beyond the typical environments is unfeasible. Hence, these models cannot be generalized to any arbitrary environment.

2) BEYOND SOTA

Addressing the limitations in current SOTA models, we enhance the ITU LoS model [32] by:

1) Allowing the UE to reside anywhere on the street, depicted in Fig. 1(b).
2) Incorporating azimuth-dependent LoS behavior, taking into account angular variations in building and street structures (see Fig. 1(c)).

Our P_{LoS} model adopts a 3D perspective to reproduce the UxNB and UE locations, allowing UxNB placement in any direction relative to the UE, as illustrated by angles (θ, φ) in Fig. 1(c). This offers a more realistic representation over current models (Figs. 1(a)).

By using the ITU-based Manhattan urban layout (see Section II), our model features adaptability across scenarios. A side-by-side comparison with existing ITU-based P_{LoS} models is available in Table 1.

Key Contributions:

- *Generalized 3D A2G P_{LoS} Model:* We present a generalized 3D A2G geometry-based P_{LoS} model for arbitrary urban environments that uses ITU-defined built-up statistical parameters, UxNB height h_M, elevation angle θ between UxNB and UE as inputs to obtain P_{LoS}. Unlike empirical models constrained to four standard urban environments, our approach accommodates any environment based on an arbitrary set of built-up parameters (α, β, γ), which shows the generalizability of the proposed model.

- *Improved Realism with Inclusion of Azimuth & all Regions:* In contrast to the existing P_{LoS} models considering a single UE position for a particular elevation angle θ, our model takes into account every conceivable UE position where no buildings are present using elevation angle θ and azimuth φ. The inclusion of both angles (θ, φ) makes the proposed model more realistic and accurate.

- *Validation Through Simulator Data:* We developed a lightweight computational simulator to validate the proposed analytical model. We compare the results of the proposed 3D model with SOTA P_{LoS} models, 3GPP P_{LoS} measurements data, and results of the simulator. The results show that the proposed P_{LoS} model agrees well with the simulator results and 3GPP measurement data for the standard suburban environments. In contrast, the SOTA P_{LoS} models deviate from the simulator results primarily due to ignoring UE location and azimuth. Furthermore, the proposed model shows good agreement with the simulator results for different arbitrary environments.

- *Real-world Application:* Using Cologne City as a benchmark, we demonstrate the model's efficiency in delivering accurate P_{LoS} estimates for real urban environments.

The remainder of this paper is structured as follows. Section II discusses the geometrical city layout. Section III presents the proposed 3D P_{LoS} model, and Section IV introduces the geometry-based simulator. Section V compares the results of the proposed 3D and SOTA P_{LoS} models. Finally, Section VI concludes the work.

TABLE 1. Comparison of the proposed and existing ITU-based PLoS models.

Model	Description	θ, h and d	Azimuth φ	UE/ UxNB Locations	Generalizability	Multi-building Blockage
[32]	The inaugural model introduced by the ITU for evaluating P_{LoS} in urban environments, using built-up parameters.	✓	—	—	✓	✓
[25]	A mathematical model to determine the optimal altitude for Low-altitude Aerial Platforms (LAPs) to maximize ground coverage, along with a closed-form P_{LoS} equation for LAPs and ground receivers	✓	—	—	—	✓
[28]	A stochastic P_{LoS} A2D model for four standard urban environments, considering frequency, h, and building width. Moreover, an approximate parametric model is built with machine learning to estimate the model parameters for a closed-form expression.	✓	—	—	✓	✓
[29]	Three stochastic probability models for LoS, GS, and BS paths in four standard urban environments. These models are based on geometric information and factors like building dimensions, frequencies, and h.	✓	—	—	✓	✓
[26]	A model that provides fitting parameters to estimate P_{LoS} for four standard environments in UAV communications, considering θ, h and d.	✓	—	✓	—	✓
[30]	A model that provides the lower and upper bounds on the P_{LoS} in terms of obstruction caused by the closest building.	✓	—	✓	✓	—
Proposed Model	The proposed generalized 3D A2G P_{LoS} model that supports diverse urban environments, based on any set of ITU-defined parameters, h, and angles (θ, φ).	✓	✓	✓	✓	✓

h = UxNB height, d = distance between UxNB and UE.

TABLE 2. Built-up Parameters for standard environments.

Environment	α	β (buildings/km^2)	γ (m)
Suburban	0.1	750	8
Urban	0.3	500	15
Dense Urban	0.5	300	20
Urban High-rise	0.5	300	50

II. GENERIC LAYOUT OF BUILT-UP ENVIRONMENTS

Based on the ITU [32], this paper considers a Manhattan grid-type urban layout built using three parameters:

- α is the ratio of land covered by buildings to the total area.
- β is the mean number of buildings per unit area.
- γ is a parameter determining the building height.

Here, γ is the scale parameter of the Rayleigh distribution to generate random building heights h_B using

$$f(h_B) = \frac{h_B}{\gamma^2} \exp\left(-\frac{h_B^2}{2\gamma^2}\right). \tag{1}$$

We can generate an arbitrary city geometry/layout by adjusting these built-up parameters, as illustrated in Fig. 2. Table 2 outlines the built-up parameters for four typical urban environments (considered in [25], [26], [28], [29], [32]). As indicated in Fig. 2, we consider 3D buildings
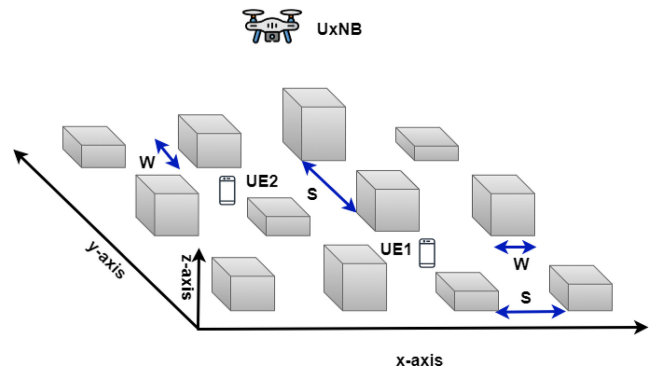
FIGURE 2. A 3D view of urban layout generated by built-up statistical parameters.

with the same length and width W. Furthermore, all the buildings are assumed to be equidistantly spaced, with the street width S. The streets are structure-free places where a UE can be located. The values of S and W depend on the reconfigurable environment or built-up parameters and are calculated using:

$$W = 1000\sqrt{\frac{\alpha}{\beta}}, \tag{2}$$

$$S = \frac{1000}{\sqrt{\beta}} - W. \tag{3}$$

Suppose a UxNB is flying at h_M, and the UE_i is located at a distance d_i. If there are n buildings between UxNB and UE, the link between both entities is considered Non-LoS (NLoS) if any of n buildings obstruct the direct path. Otherwise, the link would be in LoS. Generally, the buildings in urban areas cause major obstructions. Therefore, our P_{LoS} model considers only buildings as LoS obstruction points and ignores other objects, such as trees, towers, and vehicles. Based on these assumptions, we aim to develop a 3D geometry-based model presented in the following sections.

III. ANALYTICAL LOS PROBABILITY MODELING

This section delves into the step-by-step derivation of our proposed 3D LoS model. Building upon the existing ITU-inspired model, we introduce enhancements to improve its applicability. The derivation process is divided into distinct stages, each addressing a specific aspect of the model's improvement.

We start by revisiting the 2D elevation and height scenario presented in the ITU model. However, we extend this foundation by accommodating a more diverse environment where the UE can be located anywhere between buildings, as opposed to a fixed position in the ITU model. This enhancement is introduced gradually, initially demonstrated with a simplified example involving a single building, and then expanded to encompass scenarios with multiple buildings.

Subsequently, we move beyond the confines of 2D by introducing a 3D perspective. This is achieved through the consideration of azimuth-dependent S and W, further contributing to the model's precision and versatility.

The following sections provide a detailed breakdown of each stage in the derivation process, illustrating how our model captures the complexities of urban environments and offers a more accurate P_{LoS} estimation. At the same time, Table 3 defines all the parameters used in the model.

A. IMPACT OF THE UE LOCATION

The angle θ between the UxNB and UE is critical for P_{LoS} estimation. Fig. 3 illustrates the LoS and NLoS regions for a fixed θ. Suppose a UxNB is flying at an altitude h_M, and all the UEs are uniformly distributed over the streets. Then, one or multiple buildings can disrupt the direct link between the UxNB and UE in the street for a particular θ, as illustrated in the figure. It results in creating a building shadow for a particular height h_{B_i} and θ. Hence, no UE in this shadow region (indicated by red) has the LoS link. In contrast, all the UEs in the non-shadowed blue region are in LoS. The shadow proportion depends on the θ, W, S, and buildings' height h_B. Obviously, the final P_{LoS} also depends on the distribution of UE locations on the street. In this work, we assume a uniform distribution for UE locations. In the following subsections, we evaluate LoS obstruction caused by single and multiple buildings to derive P_{LoS} theoretically.

TABLE 3. Definitions of parameters used in the model.

| Parameter	Definition
α	Ratio of land covered by buildings to the total area
β	Mean number of buildings per unit area
γ	Rayleigh scale parameter determining the building height
A	Area occupied by three regions
d	Distance between UxNB and UE
h_{Bi}	Random ith-building height
h_{Bmax_i}	Maximum ith-building height for NLoS condition for all UEs
h_{Bmin_i}	Maximum height of the ith-building for LoS connectivity for all UEs
h_M	UxNB height
M	Azimuth Range
n	Number of obstructing buildings between UxNB and UE
$P_{\text{LoS}}^{\text{3D}}$	Resultant 3D probability of line of sight
$P_{\text{LoS}}^{\text{n}}$	Combined probability of line of sight in the presence of n obstructing building
$P_{\text{LoS}}^{\text{s}}$	Probability of line of sight in the presence of a single obstructing building
$P_{\text{LoS}_i}^{\text{s}}$	Probability of line of sight in the presence of a single obstructing ith-building
$P_{\text{LoS}}^{\text{Ri}}$	Probability of line of sight for ith-Region
P_{part_i}	Partial LoS condition when $h_{\text{Bmin}_i} < h_{B_i} < h_{\text{Bmax}_i}$
P_{pure_i}	Pure LoS condition when $h_{B_i} < h_{\text{Bmin}_i}$
S	Standard street width
S'	Effective street width against φ
S'_{R_i}	Effective street width for ith-Region
W	Standard building width
W'	Effective building width against φ
R_i	ith-Region
φ	Azimuth
θ	Elevation angle
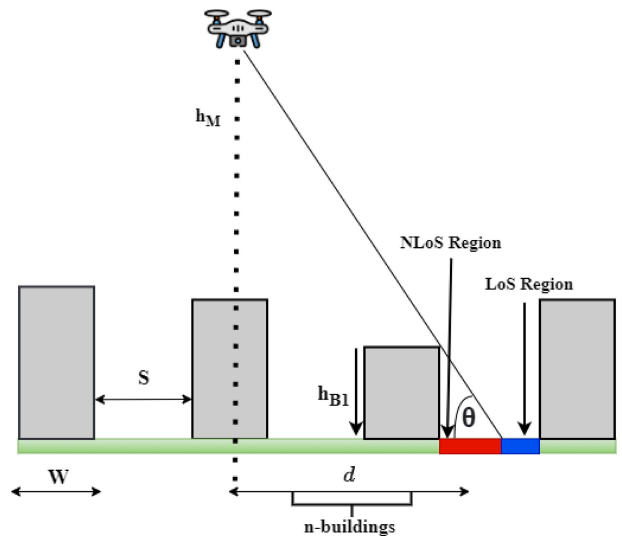
FIGURE 3. The LoS and NLoS regions for a certain θ.

B. OBSTRUCTION BY A SINGLE BUILDING

To begin, we delve into the influence of a single building nearest the UE. We set the UE height as $h_U = 0$ for the sake
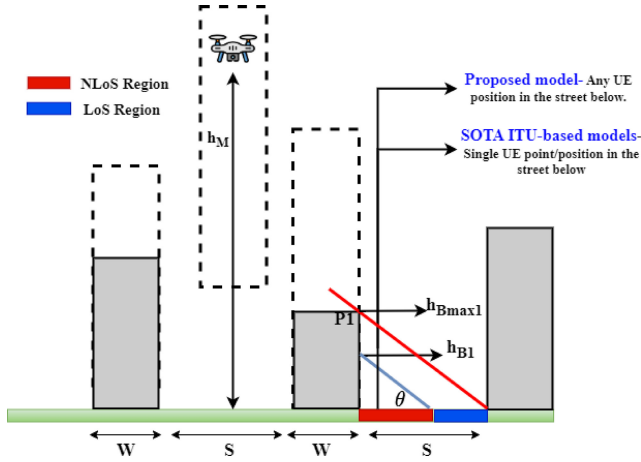
FIGURE 4. Obstruction caused by a single building between UxNB and UE.

of simplicity. The heights of these buildings conform to a Rayleigh distribution with scale parameters γ, resulting in the buildings adopting diverse heights within the dotted area as depicted in Fig. 4. Similarly, the UxNB has the freedom to navigate at varying altitudes, visualized by the dotted region in the figure. For a specific θ, there exists a building of height h_{Bmax_1} (consider P1), which is the maximum building height that casts a shadow on the entire street, as given by the red line in Fig. 4. As a result, all UEs on the street would be in NLoS. The h_{Bmax_1} is calculated as

$$h_{\text{Bmax}_1} = S\tan(\theta). \tag{4}$$

If the actual height of the closest building to the UE is $h_{\text{B}_1} < h_{\text{Bmax}_1}$, as indicated by the sky blue line, then all the UEs below the sky blue line in the red region would be in NLoS, and others would be in LoS. In this work, we assume the UE location to be uniformly distributed in $\mathcal{U}[0, S]$, as shown in Fig. 4. Thus, P_{LoS} in the presence of a single building ($P_{\text{LoS}}^{\text{s}}$) can be calculated as [34]

$$P_{\text{LoS}}^{\text{s}}(\theta, S, W) = \frac{1}{S}\int_0^S\int_0^{h_{\text{Bmax}_1}} \frac{h_{\text{B}}}{\gamma^2}e^{\frac{-h_{\text{B}}^2}{2\gamma^2}} \, dh_{\text{B}}dS, \tag{5}$$

The closed-form expression of (5) is presented as

$$P_{\text{LoS}}^{\text{s}}(\theta, S, W) = 1 - \sqrt{\frac{\pi}{2}}\frac{\gamma}{h_{\text{Bmax}_1}}\text{erf}\left(\frac{h_{\text{Bmax}_1}}{\sqrt{2}\gamma}\right), \tag{6}$$

the derivation of the above expression is given in Annex A.

This expression is valid for the single closest building obstructing LoS for UEs uniformly distributed over the street. In reality, there are n buildings between UxNB and UE to influence P_{LoS}. Therefore, the following Section explains the impact of multiple buildings on P_{LoS}.

C. OBSTRUCTION BY MULTIPLE BUILDINGS

Fig. 5 provides a visual representation of the process to calculate the P_{LoS} when dealing with multiple buildings. Now focus on the second building, with a height of h_{Bmax_2} at point P2. This building's presence creates a shadow that
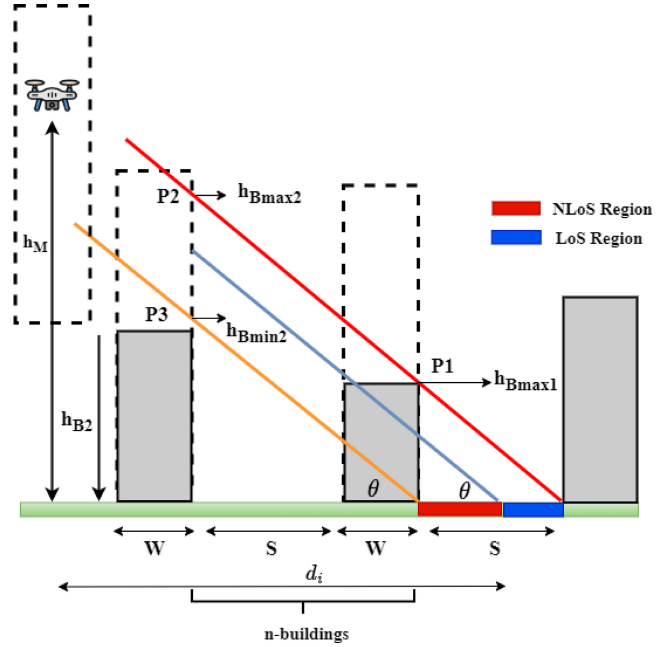

FIGURE 5. Obstruction caused by multiple buildings between UxNB and UE.

covers the entire observed street width, as indicated by the red line in Fig. 5. Hence, for any building height $h_{\text{Bmax}_2} > h_{\text{Bmax}_2}$, it will block the entire street, resulting in a complete NLoS for all UEs in that street.

On the contrary, if the height of the second building does not exceed h_{Bmin_2} (as described in P3), it will not cast a shadow on the street under observation, as illustrated by the orange line. It signifies that all UEs will maintain the LoS connectivity on the observed street, provided that the height of the building h_{B_2} does not surpass h_{Bmin_2}. We denote this phenomenon as P_{pure_i}, and it is characterized by the condition where $h_{\text{B}_2} < h_{\text{Bmin}_2}$, resulting in a 100% P_{LoS}. Mathematically, P_{pure_i} can be expressed as follows:

$$P_{\text{pure}}^{\text{s}}(\theta, S, W)_i = \int_0^{h_{\text{Bmin}_i}} \frac{h_{\text{B}}}{\gamma^2}e^{\frac{-h_{\text{B}}^2}{2\gamma^2}} \, dh_{\text{B}} \tag{7}$$

A noteworthy point to mention is that in the case of a single obstructing building, the concept of P_{pure_i} does not apply since h_{Bmin_1} equals zero.

When dealing with building heights ranging between h_{Bmin_2} and h_{Bmax_2}, the situation becomes more complicated, as represented by the sky blue line. Within this interval, we get partial street coverage or shadow. As a result, the UEs in the street may or may not maintain a LoS connection. We define this intermediate state as P_{part_i}, and its calculation is as follows:

$$P_{\text{part}}^{\text{s}}(\theta, S, W)_i = \frac{1}{S}\int_0^S\int_{h_{\text{Bmin}_i}}^{h_{\text{Bmax}_i}} \frac{h_{\text{B}}}{\gamma^2}e^{\frac{-h_{\text{B}}^2}{2\gamma^2}} \, dh_{\text{B}}dS \tag{8}$$

Hence, the total overall P_{LoS_i} caused by i-th building can be written as a sum of P_{pure_i} and P_{part_i}:

$$P_{\text{LoS}}^{\text{s}}(\theta, S, W)_i = P_{\text{pure}}^{\text{s}}(\theta, S, W)_i + P_{\text{part}}^{\text{s}}(\theta, S, W)_i$$

$$P^{\mathrm{s}}_{\mathrm{LoS}}(\theta, S, W)_i = \int_0^{h_{\mathrm{Bmin}_i}} \frac{h_{\mathrm{B}}}{\gamma^2} e^{\frac{-h_{\mathrm{B}}^2}{2\gamma^2}} \, dh_B$$
$$+ \frac{1}{S} \int_0^S \int_{h_{\mathrm{Bmin}_i}}^{h_{\mathrm{Bmax}_i}} \frac{h_{\mathrm{B}}}{\gamma^2} e^{\frac{-h_{\mathrm{B}}^2}{2\gamma^2}} \, dh_B dS \quad (9)$$

It is important to mention that equation (9) is a generalized form of equation (5) for any *ith*-building. In the case of the closest building to the street where $h_{\mathrm{Bmin}_1} = 0$, equation (9) essentially simplifies to equation (5). The closed-form expression of (9) is presented in (10), and derivation is given in Annex B.

$$P^{\mathrm{s}}_{\mathrm{LoS}}(\theta, S, W)_i = 1 - \sqrt{\frac{\pi}{2}} \frac{\gamma}{h_{\mathrm{Bmax}_1}}$$
$$\times \left(\mathrm{erf}\left(\frac{h_{\mathrm{Bmax}_i}}{\sqrt{2}\gamma} \right) - \mathrm{erf}\left(\frac{h_{\mathrm{Bmin}_i}}{\sqrt{2}\gamma} \right) \right), \quad (10)$$

where, the $\kappa 1_i$, $\kappa 2_i$, h_{Bmin_i} and h_{Bmax_i} are calculated for the *i*-th building using:

$$\kappa 1_i = (i - 1) \times (S + W),$$
$$\kappa 2_i = \kappa 1_i + S, \quad (11)$$

and

$$h_{\mathrm{Bmin}_i} = \kappa 1_i \tan(\theta),$$
$$h_{\mathrm{Bmax}_i} = \kappa 2_i \tan(\theta). \quad (12)$$

$P^{\mathrm{s}}_{\mathrm{LoS}_i}$ provides the P_{LoS} expression for a single obstructing *ith*-building between UxNB and UE. In practice, there may reside multiple obstructing buildings n between a flying UxNB and a UE. Therefore, to calculate the overall P_{LoS}, encompassing all these obstructing buildings, we utilize a composite approach by multiplying the individual probabilities of obstruction introduced by each building:

$$P^{\mathrm{n}}_{\mathrm{LoS}}(\theta, S, W) = \prod_{i=1}^{n} P^{\mathrm{s}}_{\mathrm{LoS}}(\theta, S, W)_i, \quad (13)$$

n can be calculated for a UxNB flying at h_M with a particular θ with UE using $n = \lfloor \frac{h_M}{\tan(\theta)(S+W)} \rfloor$. In this equation, $\lfloor \cdot \rfloor$ is the floor function to ensure the number of buildings is an integer.

D. EFFECT OF AZIMUTH AND DIFFERENT UE LOCATIONS

The previous two subsections derive the P_{LoS} for 2D scenarios illustrated in Fig. 1(b). However, a more realistic 3D scenario is described in Fig. 1(c). Here, the UE can be positioned anywhere within the street or crossroad. At the same time, the UxNB holds the flexibility to navigate across various azimuth angles φ. Therefore, this subsection models 3D scenario is described in Fig. 1(c).

Previous calculations show that h_{Bmax_i} and P_{LoS} are derived from S and W. However, the effective street width and building width changes with respect to the locations of UxNB and UE. Therefore, it is critical to incorporate a
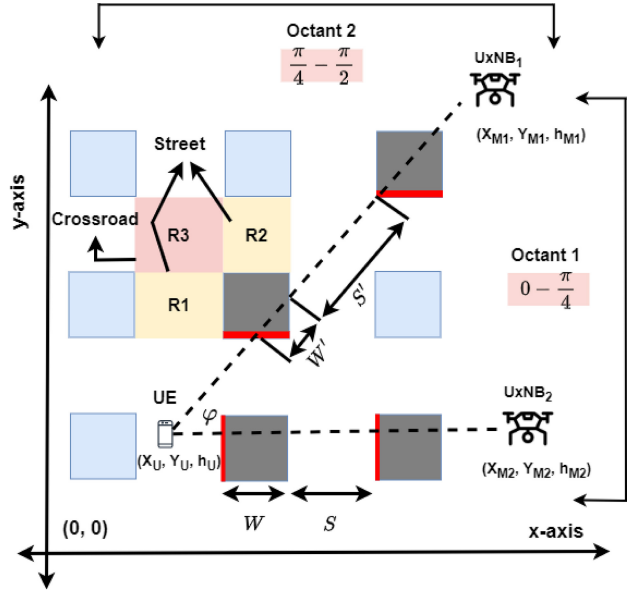

FIGURE 6. Overview of the geometry-based simulator.

horizontal angle φ between UxNB and UE that controls the effective street and building width.

Fig. 6 explains how S changes with different φ considering arbitrary locations of UxNB and UE. Suppose two UxNBs (UxNB$_1$ and UxNB$_2$) flying at altitudes h_M make the same θ with a UE in an urban environment. Suppose the azimuth between UxNB$_2$ and UE becomes zero ($\varphi = 0$); it generates regular S and W, as illustrated in Fig. 6. In contrast, azimuth between UxNB$_1$ and UE differs, resulting in a different or effective Street width S' and building Width W', as illustrated in Fig. 6. The effective S' and W' are relatively larger than standard values in the visualized scenario; thus, the P_{LoS} will also differ. The existing P_{LoS} models do not incorporate this behavior, making them less realistic.

To understand the S' and W' behavior, we take advantage of city symmetry and classify the city layout into three regions (R1, R2, R3) for possible UE locations, as shown in Fig. 6. The effective widths at these regions can be well approximated as a function of

$$S'_{R_i}(\varphi) = \begin{cases} S + 2S \tan(\varphi), & \text{for } i = 1 \\ S + 2S \cot(\varphi), & \text{for } i = 1, 2 \end{cases} \quad (14)$$

$$W'(\varphi) = \frac{W}{\cos(\varphi)}. \quad (15)$$

For simplicity and using city symmetry, we are only considering the S' and W' in the octant 1 with a range of $[0, \frac{\pi}{4}]$. The other octants follow the same S' and P_{LoS} distribution. For example, S' equals to S at $\varphi = 0$ for a UE in R1. However, it will increase when φ approaches to $\frac{\pi}{4}$. The UEs in R2 follow the opposite street pattern where S' approaches infinity at $\varphi = 0$ and decreases when it approaches $\varphi = \frac{\pi}{4}$. The R3 expression can be derived from R1 and R2. By introducing (15) in (13), we obtain the
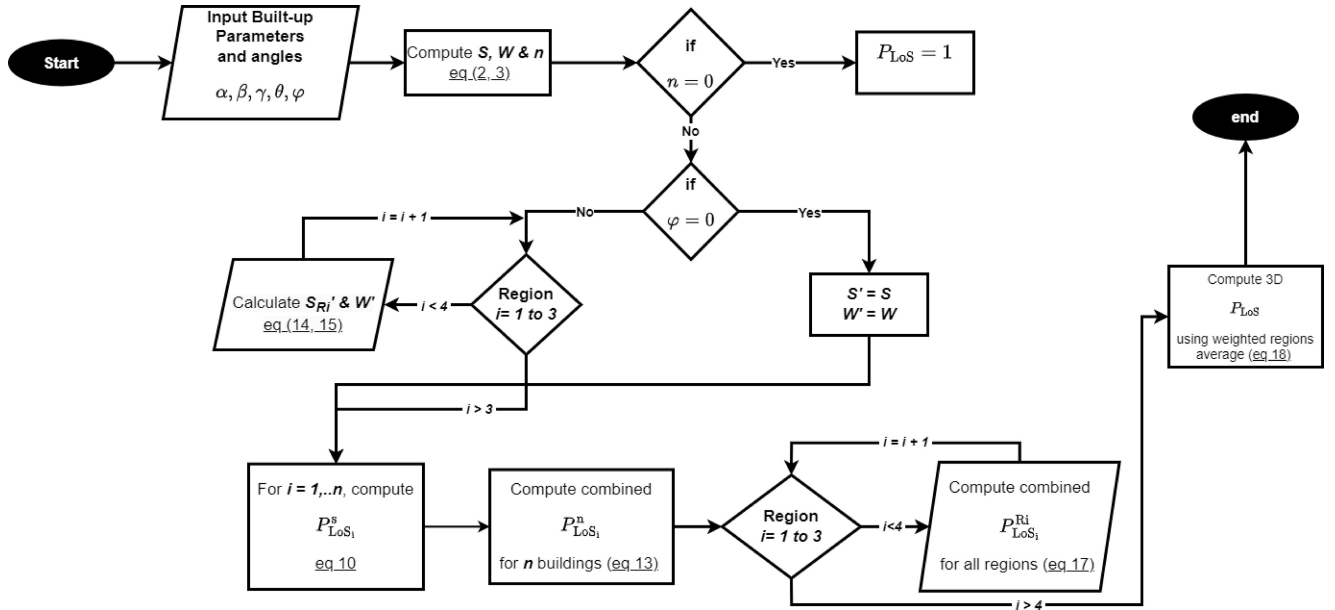
FIGURE 7. Flow chart of the proposed 3D P_{LoS} model.

resulting 3D P_{LoS} for i-th region Ri:

$$P_{\text{LoS}}^{\text{Ri}}(\theta, S, W, \varphi) = \prod_{i=1}^{n} P_{\text{LoS}}^{\text{s}}(\theta, S'_{Ri}, W')_i \qquad (16)$$

The equation (16) calculates the P_{LoS} for arbitrary values of θ and φ. Here, S'_{Ri} and W' denote the effective street and width associated with the i-th region within an octant. However, existing models currently lack the capability to compute PLoS as a function of both θ and φ.

In this context, we propose the computation of an averaged S' for varying φ to derive average 3D P_{LoS} in relation to θ for a fair comparison with existing PLoS models. Thus, integrating the right side of (16) for all the values of φ ($M = \frac{\pi}{4}$) provides the expression to estimate $P_{\text{LoS}}^{\text{Ri}}$ as a function of θ.

$$P_{\text{LoS}}^{\text{Ri}}(\theta, S, W) = \frac{1}{M} \int_{0}^{M} P_{\text{LoS}}^{\text{n}}(\theta, S'_{Ri}, W', \varphi) d\varphi, \quad (17)$$

The provided equation calculates the P_{LoS} for a specific region. Nonetheless, it is worth noting that there exist three distinct regions, as depicted in Fig. 6. The total area A occupied by three regions is $(S + W)^2 - W^2$. Therefore, the resultant 3D P_{LoS} would be the sum of the probability of the particular region multiplied by its corresponding probability:

$$P_{\text{LoS}}(\theta, S, W) = \frac{SW}{A}(P_{\text{LoS}}^{\text{R1}} + P_{\text{LoS}}^{\text{R2}}) + \frac{S^2}{A}(P_{\text{LoS}}^{\text{R3}}). \quad (18)$$

E. LOS PROBABILITY MODEL BASED ON ITU BUILT-UP PARAMETERS

To simplify the direct usage of the model with the environmental parameters defined by ITU, let us reformulate (10).

By using equation (2) and (3), equation (10) can be reformulated as

$$P_{\text{LoS}}^{\text{s}}(\alpha, \beta, \gamma, \theta)_i = 1 - \frac{\gamma \sqrt{\pi/2}}{\Upsilon 2_i \tan(\theta)}$$
$$\times \left(\text{erf}\left(\frac{\Upsilon 2_i \tan(\theta)}{\sqrt{2}\gamma} \right) - \text{erf}\left(\frac{\Upsilon 1_i \tan(\theta)}{\sqrt{2}\gamma} \right) \right), \quad (19)$$

where

$$\Upsilon 1_i = \frac{1000(i - 1)}{\sqrt{\beta}},$$
$$\Upsilon 2_i = \frac{1000(i - \sqrt{\alpha})}{\sqrt{\beta}}. \qquad (20)$$

Similarly, we can reformulate equations (14), (15), (17) and (18) to obtain the resultant $P_{\text{LoS}}^{\text{3D}}$ as a function of built-up parameters and θ. For a better understanding, a complete flow chart of the proposed P_{LoS} model is given in Fig. 7

IV. GEOMETRY-BASED 3D LOS PROBABILITY SIMULATOR

In contrast to the SOTA simulators building the whole city environment, the geometry-based 3D simulator is designed to create only relevant city portions between UxNB and UE. Our analysis shows that creating only obstructing buildings does not impact P_{LoS} [33]. This process makes the simulator lightweight and scalable, which is helpful in examining P_{LoS} in larger cities or for the UEs placed at larger distances:

Firstly, the simulator places UE in the free space of the city with uniform probability. The free space is classified into a street or a crossroad region, as shown in Fig. 6. Furthermore, the UE height is assumed to be zero for simplicity. *Secondly*, a UxNB location is generated at h_M using UE's coordinate, θ, and φ. The h_M is uniformly distributed in [0, 500] m, and φ is uniformly distributed in [0, $\frac{\pi}{2}$] (by taking advantage of city
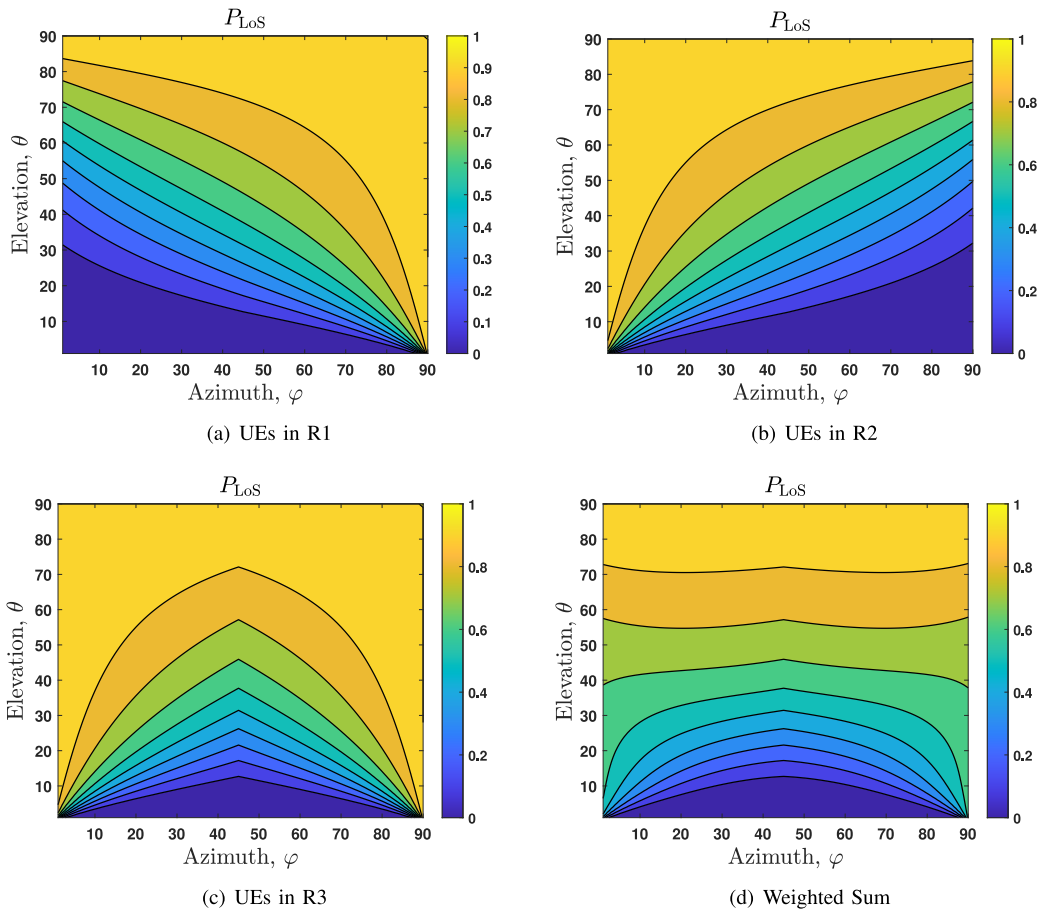
(a) UEs in R1

(b) UEs in R2

(c) UEs in R3

(d) Weighted Sum

FIGURE 8. 3D P_{LoS} analysis in the standard ITU urban environment for different UE locations by incorporating φ and θ.

symmetry). *Thirdly*, we create relevant buildings (indicated in grey in Fig. 6) between UE and UxNB with random heights that follow the Rayleigh distribution. All the sky-blue buildings in the figure only show the city's symmetry. They will not be created in the simulator for computation efficiency. The direct line between UE and UxNB can hit only two possible sides of buildings, as indicated by red in Fig. 6. All the points where the ray hit the buildings are known as Obstruction Points (OPs). In the end, we calculate and compare the critical ray height $h_{LoS(i,j)}$ with the building height (i, j) at the OP_i to check the LoS or NLoS state. In the simulator, the $h_{LoS(i,j)}$ is calculated by

$$h_{LoS(i,j)} = h_M - \frac{r_{OP(i)} \times (h_M - h_{U_i})}{d_i}, \qquad (21)$$

where $r_{OP(i)}$ is the distance between UxNB and i-th obstructing point, and h_{U_i} is UE$_i$ height. The following section presents the 3D simulator results to validate the proposed analytical P_{LoS} model.

V. VALIDATION AND RESULTS
This Section compares the proposed analytical P_{LoS} model with the 3D geometry-based simulator and SOTA models.

A. IMPACT OF AZIMUTH AND UE LOCATIONS
Fig. 8 plots the P_{LoS} against θ and φ for UE locations in three different regions. Previous SOTA P_{LoS} models [11], [25], [28], [29], [32] always assume that a UE is located in R1 with $\varphi = 0$, which represents a limiting scenario. The plotted results in Fig. 8(a) demonstrate significant variations in P_{LoS} as φ changes. For instance, if $\varphi = 90$ between UE and UxNB in R1 (see Fig. 6), there will be no obstructing building between UE and UxNB. Therefore, we get 100% P_{LoS}, as shown in Fig. 8(a). In contrast, we get standard P_{LoS} at $\varphi = 90$ and 100% P_{LoS} at $\varphi = 0$ in R2, as shown in Fig. 8(b). Similarly, Fig. 8(c) represents the P_{LoS} for UEs located on a crossroad, while Fig. 8(d) illustrates the weighted sum P_{LoS} across all regions, as given in equation (18). In conclusion, P_{LoS} varies for same θ if φ changes. Based on the analysis above, it is evident that neglecting the UE locations and φ leads to less realistic P_{LoS} models.

To demonstrate the impact of UE location and φ, Fig. 9 plots the P_{LoS} against θ for four standard urban environments. The red and blue lines represent the proposed 3D model and simulator results, respectively, while the other three lines correspond to models from [25], [32], and [26]. Fig. 9(a) shows a good agreement for the suburban
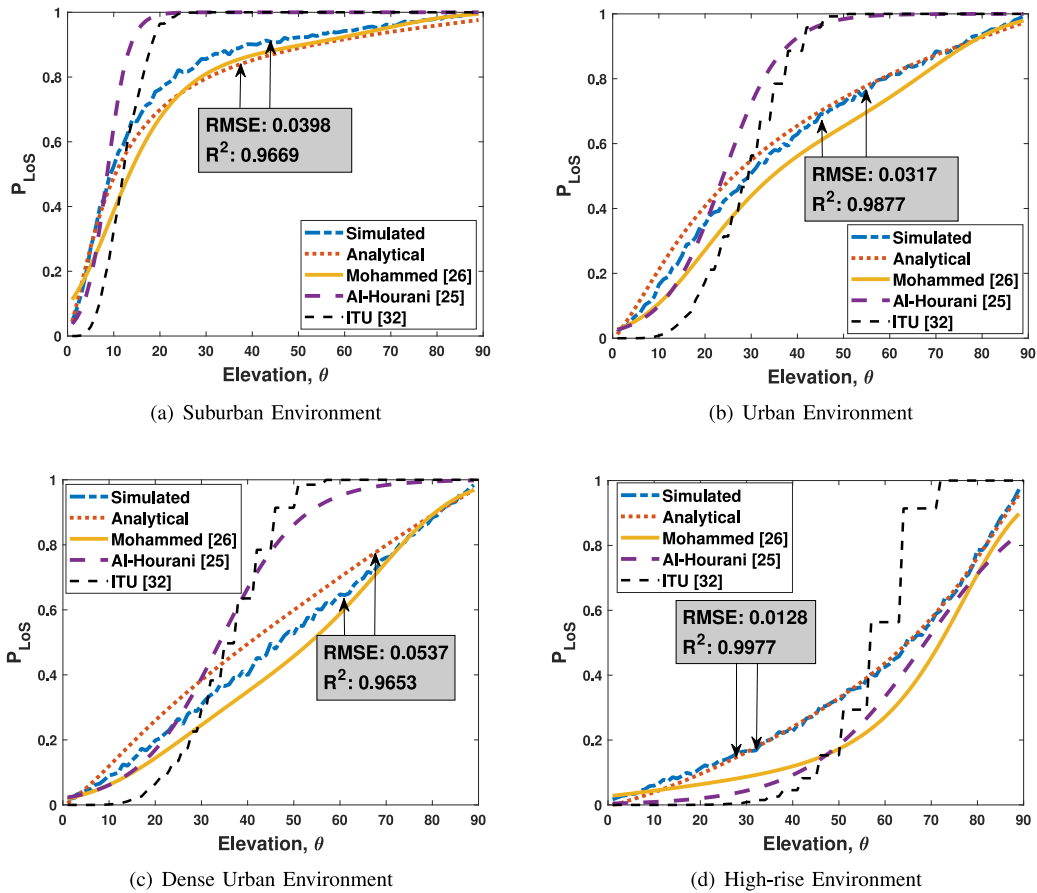
FIGURE 9. P_{LoS} of the 3D simulator and analytical model compared with existing models in four standard urban environments.

environment between the proposed simulated and analytical results with the Root Mean Square Error (RMSE) of 0.0398 and R^2 of 0.9669. The same trend can be observed in Fig. 9(b), Fig. 9(c), and Fig. 9(d), depicting urban, dense urban, and high-rise environments, respectively. The average RMSE and R^2 between the analytical model and simulated results for four standard environments are 0.0345 and 0.9794, respectively. The disparity between the proposed P_{LoS} model and existing P_{LoS} models is due to overlooking φ and UE locations.

B. GENERALIZABILITY

To demonstrate the generalizability of the proposed model, Fig. 10 plots P_{LoS} for four arbitrary environments created using random built-up parameters (α, β, γ). The figure compares the simulator results with the proposed analytical P_{LoS} model, ITU model [32] and Al-Hourani model [25]. The graphs show a significant mismatch between the simulated, ITU, and Al-Hourani model results. The primary reason for such a mismatch is considering a less realistic scenario, as mentioned in Fig. 1(a).

In contrast, the results offer a good agreement between the simulated and analytical results of four listed arbitrary environments with average RMSE and R^2 values of 0.0343 and 0.9825. In the same way, we tested our model over

50 arbitrary environments by using different values of built-up parameters; each simulated over 1000 iterations for averaging. The results show average RMSE and R^2 values of 0.0400 and 0.9735, respectively. These findings emphasize how well the proposed model can estimate P_{LoS} for any set of built-up parameters (α, β, γ).

To analyze the applicability of the proposed P_{LoS} model, we compare the analytical model and simulator findings with 3GPP measurements in a suburban environment [35], as demonstrated in Fig. 11. We can easily estimate the built-up parameters for such an environment ($\alpha = 0.1$, $\beta = 200$, $\gamma = 8$) using the fitting as in [11], as 3GPP does not explicitly provide them. The results show a good agreement with measurements. In contrast, the P_{LoS} model in [26] cannot be parameterized for any environment, resulting in a mismatch as illustrated in Fig. 11.

Finally, Fig. 12 and Fig. 13 compare the P_{LoS} of the proposed model against the UE distance and UxNB height. Figure 12 pertains to an urban environment, while Figure 13 showcases the case of a high-rise urban setting. The above-mentioned figures exhibit results for a selective set of UxNB heights (100m and 300m); however, the analytical framework accommodates the utilization of arbitrary UxNB heights and UE distances for P_{LoS} estimation. The presented plots in both figures show consistency between
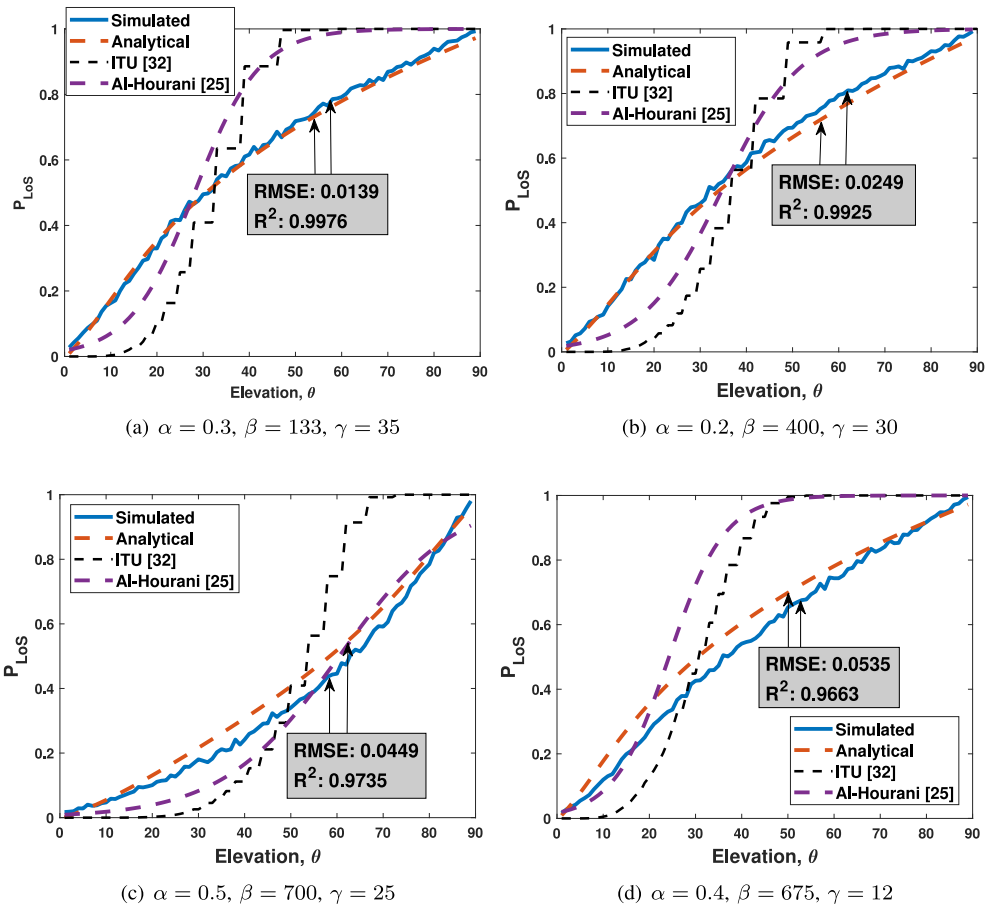
(a) $\alpha = 0.3$, $\beta = 133$, $\gamma = 35$

(b) $\alpha = 0.2$, $\beta = 400$, $\gamma = 30$

(c) $\alpha = 0.5$, $\beta = 700$, $\gamma = 25$

(d) $\alpha = 0.4$, $\beta = 675$, $\gamma = 12$

FIGURE 10. P_{LoS} analysis of arbitrary environments constructed using random built-up parameters.
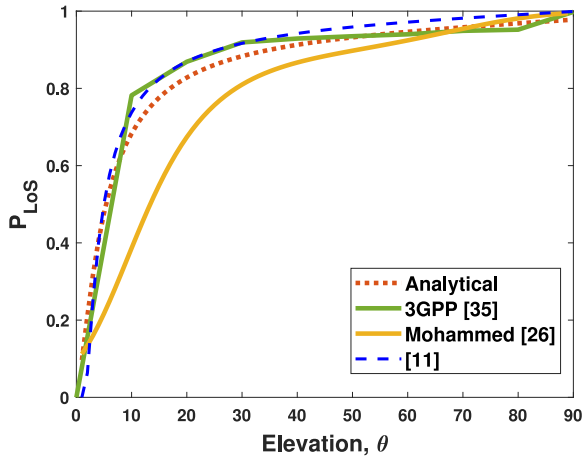

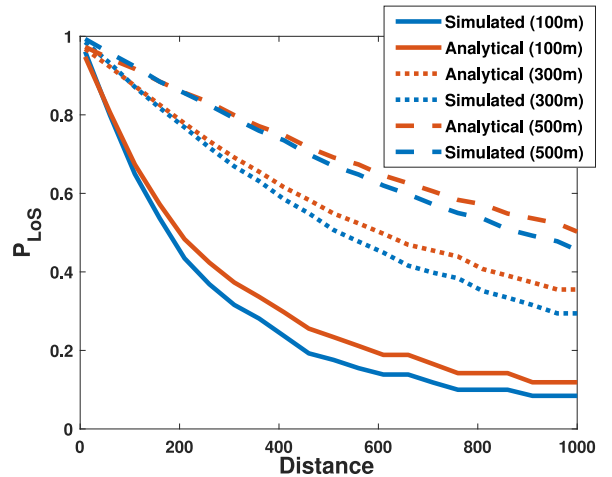**FIGURE 11.** P_{LoS} of 3GPP measurements, 3D simulator, and analytical model.

FIGURE 12. P_{LoS} of the 3D simulator and analytical model against varying UE distance and UxNB height in an urban environment.

the outcomes derived from the proposed analytical model and simulation results. This divergence from existing models can be due to their neglect of UE locations and the φ. It emphasizes the value of our comprehensive approach, capturing the significance of these factors in predicting P_{LoS}.

C. A CASE STUDY: ESTIMATING P_{LOS} IN COLOGNE CITY
This Section presents a case study that investigates the real-world applicability of our proposed P_{LoS} model, initially designed for a Manhattan-style environment. For this purpose, we picked Cologne City, located in western Germany.
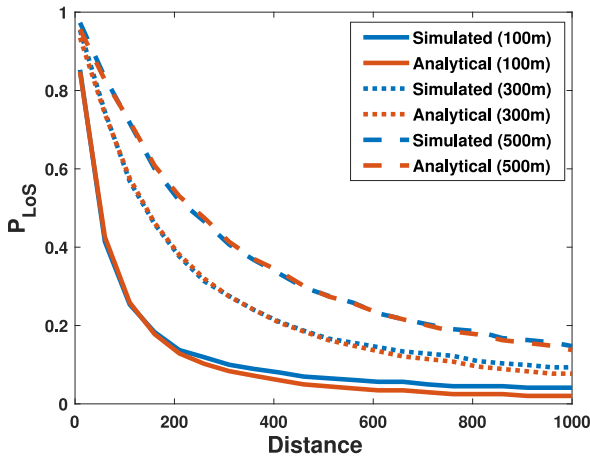
FIGURE 13. P_{LoS} of the 3D simulator and analytical model against varying UE distance and UxNB height in a high-rise environment.

FIGURE 14. Experiment Setup in Wireless InSite.

FIGURE 15. Overview of observed Cologne's urban landscape through Google Earth.

FIGURE 16. P_{LoS} analysis of Cologne City using the proposed model and results extracted through Wireless InSite.

The city's urban environment provides the backdrop for examining how useful our model is in a real urban setting. At the start, using GIS, we estimated build-up parameters for the Cologne block ($\alpha = .55$, $\beta = 680$, $\gamma = 12.69$) and plugged them into our P_{LoS} model in (19).

After that, we utilized a software called Wireless InSite [36] to facilitate this investigation. This software is known for its ability to simulate wireless communication scenarios, helping us better understand how signals behave in real-world environments. With Wireless InSite, we could study how signals interact in places like cities, considering factors such as buildings and terrain. This tool allowed us to bridge the gap between theoretical models and real-world wireless communication dynamics, enhancing the authenticity of our case study.

Wireless InSite allows users to input a 3D city or terrain for analysis. Fig. 14 shows the 3D block of the considered Cologne urban region. In contrast, Fig. 15 provides a Google Earth view of the considered region. Our investigation involved placing multiple UEs strategically, as seen by the red boxes in Figure 14. We also positioned UxNB at various locations and heights for comprehensive data collection. All the UEs getting direct rays are considered in LoS, while UEs not receiving direct rays are in NLoS.
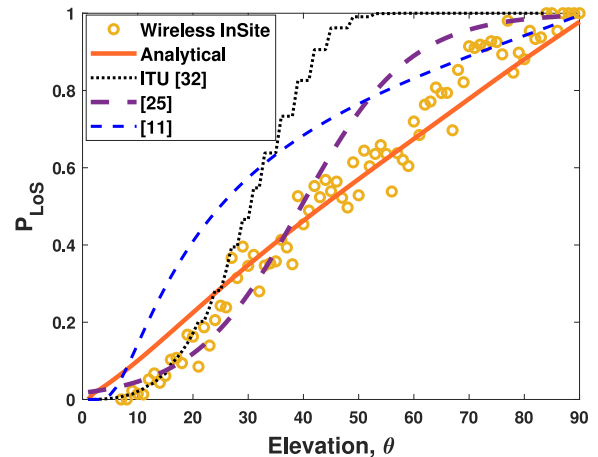
In total, we acquired more than 10,000 combinations of UE-UxNB locations. Subsequent post-processing involved calculating average LoS values corresponding to each θ. During post-processing, we could only gather P_{LoS} values for θ between $[\frac{7\pi}{180}, \frac{\pi}{2}]$. The primary reason is that creating and importing such a large city to Wireless InSite is difficult, which can give measurements for small angles ($< \frac{\pi}{36}$). It shows the benefit of using a geometry-based model over RTs.

Finally, Fig. 16 compares empirically derived P_{LoS} values using Wireless InSite to our analytical model, ITU model [32] and the models introduced in [11] and [25]. For the proposed analytical model and models in [25], [32], we use the estimated build-up parameters for Cologne. In the

TABLE 4. Performance evaluation of P_{LoS} models with RMSE and R² for Cologne.

Model	α	β	γ	RMSE	R^2
Cologne City	0.55	680	12.69	——	——
[32]	0.55	680	12.69	0.204	0.589
[25]	0.55	680	12.69	0.108	0.884
Proposed	0.55	680	12.69	0.071	0.951
[11]	$\beta = 0.3075$			0.188	0.649

case of [11], build-up parameters are not directly integrated as input parameters. Therefore, we estimated β in [11] using the build-up parameters. It is essential to mention that we only compare P_{LoS} for θ ranging between $[\frac{7\pi}{180}, \frac{\pi}{2}]$. Table 4 shows that the proposed P_{LoS} model agrees well with the Wireless InSite values with RMSE of 0.071 and R^2 of 0.951 due to considering more realistic geometry compared to SOTA models. In contrast, other models show a significant mismatch, as illustrated in Table 4. This alignment of results highlights our model's potential to offer reasonable approximations of P_{LoS} for diverse real-world environments by considering relevant built-up parameters.

VI. CONCLUSION
This study introduces an analytical model and a 3D geometry-based simulator to predict P_{LoS} in diverse urban settings defined by their distinct built-up parameters. Importantly, the proposed P_{LoS} model is applicable across any generalized urban environments for any 3D locations of UxNB and UE. Unlike existing models, the proposed 3D P_{LoS} model incorporates φ and UE locations, resulting in realistic predictions. The paper compares the proposed model and simulator with existing P_{LoS} models and 3GPP measurements. The results show a better agreement between the proposed model, measurements, and the 3D simulator, with the likelihood indicated by R^2 higher than 97%, which shows the accuracy of the proposed analytical model. Finally, a case study using Cologne City demonstrates the practical applicability of the proposed model in real-world environments.

ANNEX A: CLOSED-FORM EXPRESSION FOR OBSTRUCTION BY A SINGLE BUILDING
Given the integral:

$$P_{\text{LoS}}^{\text{s}}(\theta, S, W) = \frac{1}{S} \int_0^S \int_0^{h_{\text{Bmax}_1}} \frac{h_B}{\gamma^2} e^{\frac{-h_B^2}{2\gamma^2}} \, dh_B dS,$$

Converting $h_{\text{Bmax}_1} = S \tan(\theta)$

$$P_{\text{LoS}}^{\text{s}}(\theta, S, W) = \frac{1}{S} \int_0^S \int_0^{S \tan(\theta)} \frac{h_B}{\gamma^2} e^{\frac{-h_B^2}{2\gamma^2}} \, dh_B dS,$$

Take the inner integral first:

$$= \int_0^{S \tan(\theta)} \frac{h_B}{\gamma^2} e^{\frac{-h_B^2}{2\gamma^2}} \, dh_B,$$

Taking constant out

$$= \frac{1}{\gamma^2} \int_0^{S \tan(\theta)} h_B \cdot e^{\frac{-h_B^2}{2\gamma^2}} \, dh_B,$$

Step 1 (Use the u-Substitution): Let $u = \frac{-h_B^2}{2\gamma^2}$, then $du = \frac{-h_B}{\gamma^2} dh_B$

when $h_B = 0$, $u = 0$
when $h_B = S \tan(\theta)$, $u = \frac{-S^2 \tan^2(\theta)}{2\gamma^2}$
Integrate the values of u-substitution:

$$= \frac{1}{\gamma^2} \int_0^{\frac{-S^2 \tan^2(\theta)}{2\gamma^2}} h_B \cdot e^u \frac{\gamma^2}{-h_B} \, du,$$

$$= - \int_0^{\frac{-S^2 \tan^2(\theta)}{2\gamma^2}} e^u \, du,$$

Simplify the integral:

$$= - \left(e^u \Big|_0^{\frac{-S^2 \tan^2(\theta)}{2\gamma^2}} \right)$$

It simplifies to:

$$= 1 - e^{\frac{-\tan^2(\theta)S^2}{2\gamma^2}}$$

Step 2 (Put the Results in the Main Integral):

$$P_{\text{LoS}}^{\text{s}}(\theta, S, W) = \frac{1}{S} \int_0^S (1 - e^{-\frac{\tan^2(\theta)S^2}{2\gamma^2}}) \, dS$$

Step 3 (Distribute the Constant): Distribute the constant $\frac{1}{S}$ inside the integral:

$$= \frac{1}{S} \int_0^S 1 \, dS - \frac{1}{S} \int_0^S e^{-\frac{\tan^2(\theta)S^2}{2\gamma^2}} \, dS$$

Simplify the first integral:

$$I = \frac{1}{S}(S \Big|_0^S) - \frac{1}{S} \int_0^S e^{-\frac{\tan^2(\theta)S^2}{2\gamma^2}} \, dS$$

$$= 1 - \frac{1}{S} \int_0^S e^{-\frac{\tan^2(\theta)S^2}{2\gamma^2}} \, dS$$

Step 4 (Express in Terms of Error Function): From [37], we know that

$$\text{erf(x)} = \frac{2}{\sqrt{\pi}} \int_0^x e^{-t^2} \, dt$$

Make a substitution $t = \frac{S \tan(\theta)}{\sqrt{2}\gamma}$, $dt = -\frac{\tan(\theta)}{\sqrt{2}\gamma} dS$:

$$= 1 - \frac{\sqrt{2}\gamma}{S \tan(\theta)} \int_{\frac{S \tan(\theta)}{\sqrt{2}\gamma}}^0 e^{-t^2} \, dt$$

Multiply and divide the integral by $\frac{2}{\sqrt{\pi}}$ and recognize the integral as a portion of the error function:

$$= 1 - \frac{\sqrt{2}\,\gamma}{S \tan(\theta)} \frac{\sqrt{\pi}}{2} \text{erf}\left(\frac{\tan(\theta)S}{\sqrt{2}\gamma} \right)$$

Step 5 (Final Result): Substitute back into the original expression:

$$P_{\text{LoS}}^{\text{s}}(\theta, S, W) = 1 - \sqrt{\frac{\pi}{2}} \frac{\gamma}{h_{\text{Bmax}_1}} \text{erf}\left(\frac{h_{\text{Bmax}_1}}{\sqrt{2}\gamma}\right).$$

ANNEX B: CLOSED-FORM EXPRESSION FOR OBSTRUCTION BY MULTIPLE BUILDINGS

Given the integral:

$$P_{\text{LoS}}^{\text{s}}(\theta, S, W)_i = P_{\text{pure}}^{\text{s}}(\theta, S, W)_i + P_{\text{part}}^{\text{s}}(\theta, S, W)_i$$

$$P_{\text{part}}^{\text{s}}(\theta, S, W)_i = \frac{1}{S} \int_0^S \int_{h_{\text{Bmin}}}^{h_{\text{Bmax}}} \frac{h_B}{\gamma^2} e^{\frac{-h_B^2}{2\gamma^2}} \, dh_B dS,$$

Step 1 (Take the Inner Integral and Use the u-Substitution): Take the inner integral first:

$$= \int_{h_{\text{Bmin}}}^{h_{\text{Bmax}}} \frac{h_B}{\gamma^2} e^{\frac{-h_B^2}{2\gamma^2}} \, dh_B,$$

Using the *u*-distribution and following the steps in the previous subsection, we get

$$= e^{\frac{-h_{\text{Bmin}}^2}{2\gamma^2}} - e^{\frac{-h_{\text{Bmax}}^2}{2\gamma^2}}$$

Step 2 (Put the Results in the Main Integral):

$$P_{\text{part}}^{\text{s}}(\theta, S, W)_i = \frac{1}{S} \int_0^S e^{\frac{-h_{\text{Bmin}}^2}{2\gamma^2}} - e^{\frac{-h_{\text{Bmax}}^2}{2\gamma^2}} \, dS$$

Step 3 (Distribute the Constant): Distribute the constant $\frac{1}{S}$ inside the integral:

$$= \frac{1}{S} \int_0^S e^{\frac{-h_{\text{Bmin}}^2}{2\gamma^2}} \, dS - \frac{1}{S} \int_0^S e^{\frac{-h_{\text{Bmax}}^2}{2\gamma^2}} \, dS$$

By substituting the values of h_{Bmin} and h_{Bmax} form (12) and simplifying the equation, we get the final expression:

$$P_{\text{part}}^{\text{s}}(\theta, S, W)_i = e^{\frac{-h_{\text{Bmin}}^2}{2\gamma^2}} - \sqrt{\frac{\pi}{2}} \frac{\gamma}{S\tan(\theta)}$$
$$\times \left(\text{erf}\left(\frac{h_{\text{Bmax}_i}}{\sqrt{2}\gamma}\right) - \text{erf}\left(\frac{h_{\text{Bmin}_i}}{\sqrt{2}\gamma}\right) \right)$$

Step 4 (Simplifying P_{pure_i} Expression):

$$P_{\text{pure}}^{\text{s}}(\theta, S, W)_i = \int_0^{h_{\text{Bmin}_i}} \frac{h_B}{\gamma^2} e^{\frac{-h_B^2}{2\gamma^2}} \, dh_B$$

By taking the integral, we obtain

$$P_{\text{pure}}^{\text{s}}(\theta, S, W)_i = 1 - e^{\frac{-h_{\text{Bmin}}^2}{2\gamma^2}}$$

Step 5 (Final $P_{\text{LoS}}^{\text{s}}$ Expression): Summing P_{pure_i} and P_{part_i} gives us the final expression

$$P_{\text{LoS}}^{\text{s}}(\theta, S, W)_i = 1 - \sqrt{\frac{\pi}{2}} \frac{\gamma}{h_{\text{Bmax}_1}}$$
$$\times \left(\text{erf}\left(\frac{h_{\text{Bmax}_i}}{\sqrt{2}\gamma}\right) - \text{erf}\left(\frac{h_{\text{Bmin}_i}}{\sqrt{2}\gamma}\right) \right)$$

REFERENCES

[1] H. Shakhatreh et al., "Unmanned aerial vehicles (UAVs): A survey on civil applications and key research challenges," *IEEE Access*, vol. 7, pp. 48572–48634, 2019.

[2] Y. Han, H. Liu, Y. Wang, and C. Liu, "A comprehensive review for typical applications based upon unmanned aerial vehicle platform," *IEEE J. Sel. Topics Appl. Earth Observ. Remote Sens.*, vol. 15, pp. 9654–9666, Oct. 2022. [Online]. Available: https://ieeexplore.ieee.org/document/9927352

[3] H. Jiang, Z. Zhang, L. Wu, and J. Dang, "Three-dimensional geometry-based UAV-MIMO channel modeling for A2G communication environments," *IEEE Commun. Lett.*, vol. 22, no. 7, pp. 1438–1441, Jul, 2018.

[4] N. Cheng et al., "AI for UAV-assisted IoT applications: A comprehensive review," *IEEE Internet Things J.*, vol. 10, no. 16, pp. 14438–14461, Aug. 2023.

[5] S. A. H. Mohsan, M. A. Khan, F. Noor, I. Ullah, and M. H. Alsharif, "Towards the unmanned aerial vehicles (UAVs): A comprehensive review," *Drones*, vol. 6, no. 6, p. 147, 2022.

[6] A. Saboor, S. Coene, E. Vinogradov, E. Tanghe, W. Joseph, and S. Pollin, "Elevating the future of mobility: UAV-enabled intelligent transportation systems," 2021, *arXiv:2110.09934*.

[7] N. Cherif, W. Jaafar, E. Vinogradov, H. Yanikomeroglu, S. Pollin, and A. Yongacoglu, "iTUAVs: Intermittently tethered UAVs for future wireless networks," *IEEE Wireless Commun.*, vol. 30, no. 4, pp. 124–130, Aug. 2023.

[8] Z. Cui, K. Guan, C. Oestges, C. Briso-Rodríguez, B. Ai, and Z. Zhong, "Cluster-based Characterization and modeling for UAV air-to-ground time-varying channels," *IEEE Trans. Veh. Technol.*, vol. 71, no. 7, pp. 6872–6883, Jul. 2022.

[9] E. Vinogradov, H. Sallouha, S. De Bast, M. Azari, and S. Pollin, "Tutorial on UAVs: A blue sky view on wireless communication," *J. Mobile Multimedia*, vol. 14, no. 4, pp. 395–395, 2019.

[10] A. Al-Hourani, "On the probability of line-of-sight in urban environments," *IEEE Wireless Commun. Lett.*, vol. 9, no. 8, pp. 1178–1181, Aug. 2020.

[11] A. Al-Hourani and I. Guvenc, "On modeling satellite-to-ground path-loss in urban environments," *IEEE Commun. Lett.*, vol. 25, no. 3, pp. 696–700, Mar. 2021.

[12] A. A. Khuwaja, Y. Chen, N. Zhao, M.-S. Alouini, and P. Dobbins, "A survey of channel modeling for UAV communications," *IEEE Commun. Surveys Tuts.*, vol. 20, no. 4, pp. 2804–2821, 4th Quart., Jul. 2018.

[13] D. Mishra and E. Natalizio, "A survey on cellular-connected UAVs: Design challenges, enabling 5G/B5G innovations, and experimental advancements," *Comput. Netw.*, vol. 182, Dec. 2020, Art. no. 107451.

[14] G. Geraci et al., "What will the future of UAV cellular communications be? A flight from 5G to 6G," *IEEE Commun. Surveys Tuts.*, vol. 24, no. 3, pp. 1304–1335, 3rd Quart., May 2022.

[15] I. Rodriguez, H. C. Nguyen, I. Z. Kovács, T. B. Sørensen, and P. Mogensen, "An empirical outdoor-to-indoor path loss model from below 6 GHz to cm-wave frequency bands," *IEEE Antennas Wireless Propag. Lett.*, vol. 16, pp. 1329–1332, 2017.

[16] "Guidelines for evaluation of radio interface technologies for IMT-advanced," *Rep. ITU*, vol. 638, no. 31, pp. 1–72, 2009.

[17] "Study on channel model for frequency spectrum above 6 GHz (release 14)," 3GPP, Sophia Antipolis, France, 3GPP Rep. 38.900, 2017.

[18] M. K. Samimi, T. S. Rappaport, and G. R. MacCartney, "Probabilistic omnidirectional path loss models for millimeter-wave outdoor communications," *IEEE Wireless Commun. Lett.*, vol. 4, no. 4, pp. 357–360, Aug. 2015.

[19] P. Kyösti, J. Meinilä, and L. Hentilä, "WINNER II D1.1.2, V1. 2, WINNER II channel models," Inf. Soc. Technol., document IST-4-027756, 2007. [Online]. Available: https://www.researchgate.net/publication/259900906_IST-4-027756_WINNER_II_D112_v12_WINNER_II_channel_models

[20] P. Koivumäki, A. F. Molisch, and K. Haneda, "Line-of-sight probability in cluttered urban microcells: Analyses using poisson point process and point cloud," *IEEE Trans. Antennas Propag.*, vol. 70, no. 3, pp. 2161–2173, Mar. 2022.

[21] Y. Yang et al., "Real-time ray-based channel generation and emulation for UAV communications," *Chin. J. Aeronaut.*, vol. 35, no. 9, pp. 106–116, 2022.

[22] M. Lecci, P. Testolina, M. Polese, M. Giordani, and M. Zorzi, "Accuracy versus complexity for mmWave ray-tracing: A full stack perspective," *IEEE Trans. Wireless Commun.*, vol. 20, no. 12, pp. 7826–7841, Dec. 2021.

[23] T. S. Rappaport, S. Sun, and M. Shafi, "Investigation and comparison of 3GPP and NYUSIM channel models for 5G wireless communications," in *Proc. IEEE Veh. Technol. Conf. (VTC-Fall)*, 2017, pp. 1–5.

[24] J. Holis and P. Pechac, "Elevation dependent shadowing model for mobile communications via high altitude platforms in built-up areas," *IEEE Trans. Antennas Propag.*, vol. 56, no. 4, pp. 1078–1084, Apr. 2008.

[25] A. Al-Hourani, S. Kandeepan, and S. Lardner, "Optimal LAP altitude for maximum coverage," *IEEE Wireless Commun. Lett.*, vol. 3, no. 6, pp. 569–572, Dec. 2014.

[26] I. Mohammed, I. B. Collings, and S. V. Hanly, "Line of sight probability prediction for UAV communication," in *Proc. IEEE Int. Conf. Commun. Workshops (ICC Workshops)*, Montreal, QC, Canada, 2021, pp. 1–6.

[27] M. Gapeyenko, D. Moltchanov, S. Andreev, and R. W. Heath, "Line-of-sight probability for mmWave-based UAV communications in 3D urban grid deployments," *IEEE Trans. Wireless Commun.*, vol. 20, no. 10, pp. 6566–6579, Oct. 2021.

[28] Q. Zhu et al., "Geometry-based stochastic line-of-sight probability model for A2G channels under urban scenarios," *IEEE Trans. Antennas Propag.*, vol. 70, no. 7, pp. 5784–5794, Jul. 2022.

[29] M. Pang et al., "Geometry-based stochastic probability models for the LoS and NLoS paths of A2G channels under urban scenarios," *IEEE Internet Things J.*, vol. 10, no. 3, pp. 2360–2372, Feb. 2023.

[30] I. Mohammed, S. Gopalam, I. B. Collings, and S. V. Hanly, "Closed form approximations for UAV line-of-sight probability in urban environments," *IEEE Access*, vol. 11, pp. 40160–40174, 2023.

[31] H. Jiang, Z. Zhang, and G. Gui, "Three-dimensional non-stationary Wideband geometry-based UAV channel model for A2G communication environments," *IEEE Access*, vol. 7, pp. 26116–26122, 2019.

[32] *Propagation Data and Prediction Methods Required for the Design of Terrestrial Broadband Radio Access Systems Operating in a Frequency Range from 3 to 60 GHz*, ITU-Rec.R P.1410-6, Int. Telecommun. Union, Geneva, Switzerland, 2023. [Online]. Available: https://www.itu.int/dms_pubrec/itu-r/rec/p/R-REC-P.1410-6-202308-I!!PDF-E.pdf

[33] A. Saboor, E. Vinogradov, Z. Cui, and S. Pollin, "Probability of line of sight evaluation in urban environments using 3D simulator," in *Proc. IEEE Int. Black Sea Conf. Commun. Netw. (BlackSeaCom)*, 2023, pp. 135–140.

[34] Z. Cui, K. Guan, C. Briso-Rodríguez, B. Ai, and Z. Zhong, "Frequency-dependent line-of-sight probability modeling in built-up environments," *IEEE Internet Things J.*, vol. 7, no. 1, pp. 699–709, Jan. 2020.

[35] "Study on new radio (NR) to support non terrestrial networks (release 15)," 3GPP, Sophia Antipolis, France, 3GPP Rep. 38.811, 2018.

[36] "Wireless InSite," Remcom.com. Accessed: Aug. 8, 2023. [Online]. Available: https://www.remcom.com/wireless-insite-em-propagation-software

[37] E. W. Weisstein, "Erf," Wolfram.com. Accessed: Aug. 26, 2023. [Online]. Available: https://mathworld.wolfram.com/

ABDUL SABOOR received the master's degree in information technology from the National University of Sciences and Technology, Pakistan, in 2018. He is currently pursuing the Ph.D. degree with KU Leuven, Belgium. After that, he moved to the Thomas Johann Seebeck Department of Electronics, School of Information Technology, Tallinn University of Technology, to research the development and exploitation of a smart wearable-assistive neuromuscular stimulation system using data analytics. His current research investigates the design and analysis of ultra-reliable UAV-assisted vehicular communication networks. Beyond his research, he has served as a Reviewer for renowned journals and conferences, including IEEE INTERNET OF THINGS JOURNAL, IEEE COMMUNICATION LETTERS, IEEE OPEN JOURNAL OF VEHICULAR TECHNOLOGY, Bodynets 2021, and IEEE ICC 2022.

EVGENII VINOGRADOV (Member, IEEE) received the engineering degree from Saint-Petersburg Electrotechnical University and the Ph.D. degree from UCLouvain. He is a Lead Researcher with Technology Innovation Institute, UAE, and a Visiting Professor with KU Leuven, Belgium, focusing on wireless communication systems. He is currently deeply invested in exploring advancements in communication systems for Advanced Air Mobility and 6G Technology (particularly in cell-free MIMO and non-terrestrial networks).

ZHUANGZHUANG CUI (Member, IEEE) received the Ph.D. degree in electrical engineering from Beijing Jiaotong University, Beijing, China, in April 2022. He is currently a Postdoctoral Fellow with the Networked Systems, WaveCoRE, Department of Electrical Engineering, KU Leuven, Belgium. From 2019 to 2021, he was a Visiting Scholar/student at several universities, including UPM, Spain; North Carolina State University, USA; and UCLouvain, Belgium. His research interests include channel characterization and modeling, 5G-A/6G system design and performance analysis, integrated sensing and communications, and non-terrestrial networks. He is the recipient of the National Scholarship, China, in 2020, and a Postdoctoral Mandate from KU Leuven in 2022. He served as a Guest Editor for the *International Journal of Antennas and Propagations*, the TPC Co-Chair of the 3rd ACM MobiCom 2023 Workshop on ISAC for IoT, and a TPC Member for IEEE GLOBECOM, ICC, WCNC, and EuCNC.

AKRAM AL-HOURANI (Senior Member, IEEE) received the Ph.D. degree from RMIT University, Melbourne, Australia, in 2016. Previously, he worked as a Research and Development Program Manager in the satellite and telecommunication industry, where he directed industry projects valued at over U.S. $120 million. He is currently an Associate Professor and the Telecommunication Program Manager (Master's) with the School of Engineering, RMIT University. With his expertise, he is currently engaged in multiple research and industry projects related to satellite communications, synthetic aperture radar, and AI in wireless communications. He has contributed to over 93 journal articles and conference proceedings. His research interests include satellite communications, radar systems, UAV communication systems, signal processing/machine learning, and stochastic geometry. As a Lead Investigator, he played a crucial role in delivering the largest open Internet of Things network in Victoria in collaboration with five local governments, the Northern Melbourne Smart Cities Network. This project won two prestigious industry awards, such as the Technology Awards for Excellence 2020 from the Municipal Association of Victoria and the Smart Cities Award for 2020 from the IoT Alliance Australia. He was awarded the IEEE Sensors Council Paper Award for his contribution in hand-gesture recognition using neural networks. He is currently ranked in the top 2% of scientists worldwide according to Stanford University's latest rankings, in both the Career-Long and Single Year Impact categories. He is currently an Associate Editor of multiple high-impact journals, including IEEE TRANSACTIONS ON AEROSPACE AND ELECTRONICS SYSTEMS, IEEE OPEN JOURNAL OF THE COMMUNICATION SOCIETY, and *Frontiers in Space Technologies*. He is also an Editor of the *Remote Sensing* (MDPI).

SOFIE POLLIN (Senior Member, IEEE) is a Professor with KU Leuven, focusing on wireless communication systems. Before that, she worked with IMEC and UC Berkeley, and she is currently still a Principal Member of the Technical Staff with IMEC. Her research centers around wireless networks that require networks that are ever more dense, heterogeneous, battery-powered, and spectrum-constrained. Her research interests are cell-free networks, integrated communication and sensing, and non-terrestrial networks.